OBSERVATIONS OF A POST-FLARE RADIO BURST IN X-RAYS

Z. ŠVESTKA[1], R. T. STEWART[2], P. HOYNG[1], W. VAN TEND[1],
L. W. ACTON[3], A. H. GABRIEL[4], C. G. RAPLEY[5], A. BOELEE[1],
E.C. BRUNER[3], C. DE JAGER[1], H. LAFLEUR[1], G. NELSON[2],
G. M. SIMNETT[6], H. F. VAN BEEK[1], and W. J. WAGNER[7]

Abstract. More than six hours after the two-ribbon flare of 21 May 1980, the hard X-ray spectrometer aboard the SMM imaged an extensive arch above the flare region which proved to be the lowest part of a stationary post-flare noise storm recorded at the same time at Culgoora. The X-ray arch extended over 3 or more arc minutes to a projected distance of 95 000 km, and its real altitude was most probably between 110 000 and 180 000 km. The mean electron density in the cloud was close to 10^9 cm^{-3} and its temperature stayed for many hours at a fairly constant value of about 6.5×10^6 K. The bent crystal spectrometer aboard the SMM confirms that the arch emission was basically thermal. Variations in brightness and energy spectrum at one of the supposed footpoints of the arch seem to correlate in time with radio brightness suggesting that suprathermal particles from the radio noise regions dumped in variable quantities into the low corona and transition layer; these particles may have contributed to the population of the arch, after being trapped and thermalized. The arch extended along the $H_\parallel = 0$ line thus apparently hindering any upward movement of the upper loops reconnected in the flare process. There is evidence from Culgoora that this obstacle may have been present above the flare since 15–30 min after its onset.

1. Introduction

On May 21, 1980, the hard X-ray imaging spectrometer aboard the SMM (HXIS, Van Beek *et al.*, 1980) observed a major flare of importance 2B in Hα and of class X1 in 1–8 Å X-rays. HXIS acquired images of this flare in six energy bands from 3.5 through 30 keV, starting at the very beginning of the flare event. The early phase of the flare development was analyzed by Hoyng *et al.* (1981), whereas in this paper we are interested in the later – and very late – phase of the flare development.

The 21 May event was a 'classical' two-ribbon flare, initiated by a filament disruption at about 20:50 UT. The impulsive phase peaked at 20:56 UT. The Hα ribbons began to be visible at 20:55 UT, and the first bright 'post-flare' loops could be seen in Hα shortly after the flare maximum, at 21:00 UT. In >3.5 keV X-rays the first flare emission (i.e. the first flare loops) appeared at about 20:52 UT (cf.
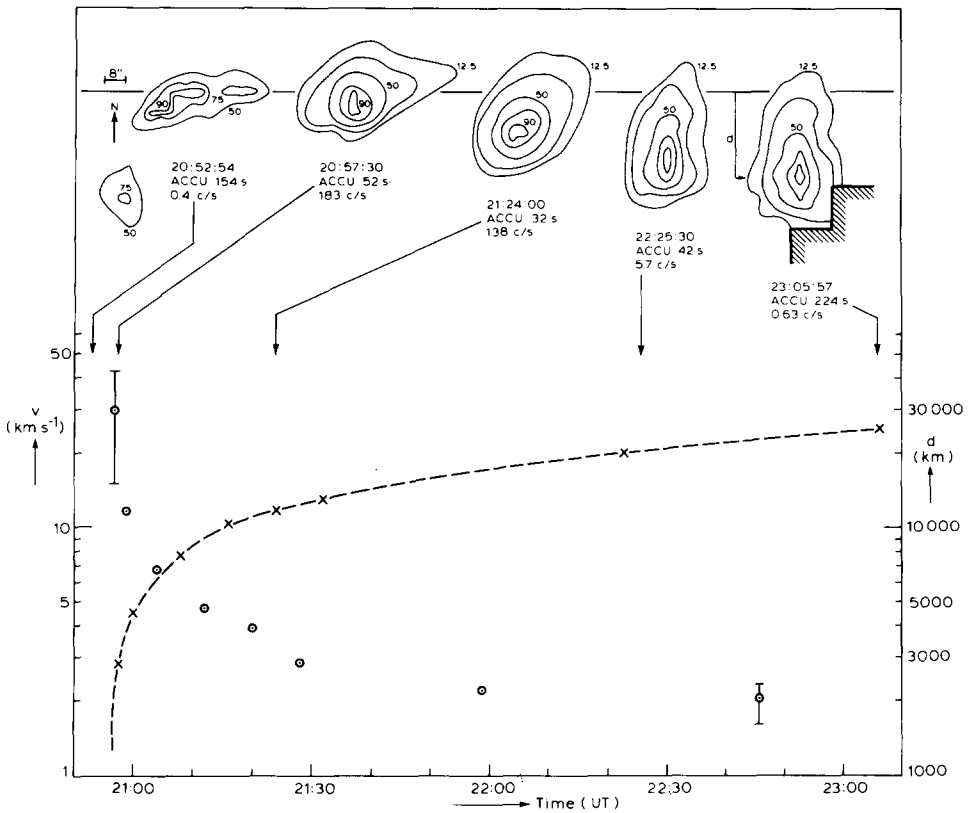
Fig. 1.   Contour plots of the flare of 21 May, 1980 in 3.5–8.0 keV X-rays at the times (= mean times of integration) indicated by arrows in the graph below. The contours are at 90, 75, 50, 25, and 12.5% of the maximum count which is given below each plot in counts per second (c/s) per 8″ × 8″ pixel. Many single HXIS images were added before constructing each contour plot, and ACCU gives the integration time in s. In the graph we show the smoothed apparent (projected) speed v of the shift of the loop tops (= maximum brightness regions) towards the south (circles), and the apparent distance d the loop tops travelled since the flare onset (crosses).

Figure 1), when some parts of the dark Hα filament had disappeared, whereas other parts were rising in the process of the filament eruption. Since that time these X-ray loops were seen continuously growing (i.e. extending towards SSW from the flare position at 15 W, 14 S) as long as HXIS looked at the region, until 23:17 UT (Figure 1).

So far we had little chance to observe the growth of the 'post-flare' loops in X-rays. The best event was seen by Skylab on 29 July 1973 (Moore *et al.*, 1979; Nolte *et al.*, 1979; Petrasso *et al.*, 1979), but those observations started 2.5 hr after the flare maximum, and only a few isolated photographs of the X-ray loop system were available. Also, all observations on Skylab were carried out at much lower energies, usually from 0.2 to 4.0 keV, with low efficiency at the upper end. (The highest available energy band was 1.1–4.0 keV.) Therefore, we will first discuss

here the growth of the X-ray loops, in energy range of 3.5–8.0 keV, in order to see to what extent these data confirm the earlier results obtained by Skylab.

2. Growth of the Flare Loops

The SMM looked at the flare in two orbits: From 20:45 through 21:35 and from 22:21 through 23:10 UT. Figure 1 shows how the shape of the flare changed in 3.5–8.0 keV X-rays during this period. At the top we present isophotes constructed from the flare images obtained in the fine field of view of HXIS, with spatial resolution of 8 arc sec. The contour plot at 23:05:57 shows the boundary of the HXIS fine field of view. The contours represent simple interpolations of counts between all neighbouring $8'' \times 8''$ pixels (in vertical, horizontal and diagonal directions).

The first contour plot, at 20:52:54 (i.e. integrated from 20:51:37 through 20:54:11) shows the X-ray enhancement at the time of the filament eruption, and the emission marks nicely the original position of the filament, i.e. the $H_\| = 0$ line in the active region (as found from comparisons with Hα photographs kindly provided to us by D. M. Rust). Thus we can use this position as a reference to the site of formation of the first flare loops.

Experience from Skylab (e.g. Nolte *et al.*, 1979) has shown that the maximum brightness in a flare-loop system is at the top of the loops. Thus, as Figure 1 shows, the first hot X-ray loops formed exactly over the $H_\| = 0$ line along which the filament had extended before, but after that the loop tops shifted gradually to the south, i.e. in the direction in which the filament material had been ejected earlier (Hoyng *et al.*, 1981).

We know, from Hα flare ribbons, that the 'post-flare' loops continuously grow in altitude. Thus the southward drift implies an altitude growth. Since the loop was located only 12 degrees south from the east–west line on the solar surface, a radial growth would correspond to initial rise in excess of 140 km s^{-1}, and to a loop altitude of $\sim 120\,000$ km at 23 UT. These values appear to be too high when compared with other similar cases. Thus the loops (and probably also the path of the erupting filament) were evidently inclined from the radial direction toward the south, but the angle α of this inclination is unknown. (See Section 4A for additional evidence and an estimate of α.)

The lower part of Figure 1 shows the growing distance d of the loop tops from the original filament channel (the real top altitude above the $H_\| = 0$ line is then $h = d/\cos(78° - \alpha)$) and the corresponding apparent speed of growth, v. (The real speed is $v/\cos(78° - \alpha)$.) We give here smoothed values of v and d, obtained from 12 sets of X-ray flare contours, by comparing in each pair the 90% and 75% isophotes at their northern and southern edges. Thus we get four measurements for each pair, and the typical scatter of these measured values is demonstrated by error bars for the earliest, and the latest values of v in Figure 1. The errors are

large in the early phase of the flare because of the short time intervals in combination with fast changes in the loop-system at the beginning of the flare.

Figure 1 demonstrates that the hot X-ray loops were still clearly visible at the end of HXIS observations of the flare, more than two hours after the flare maximum, and at that time the loops were still growing, with an apparent (projected) speed of 1.5–2.0 km s^{-1}.
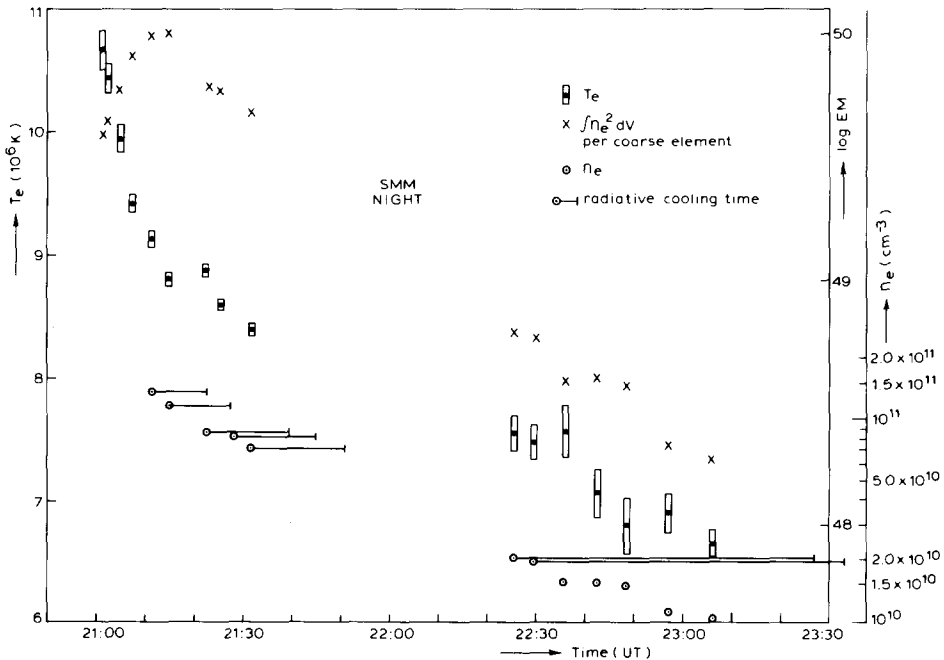

Fig. 2.   Effective temperature T_e and emission measure EM per one coarse element $(32 \times 32'')$ as determined from the ratio of counts in the 3.5–8.0 keV energy bands. The error bars represent $\pm 1\sigma$ deviations. The coarse element with maximum count rate was considered at all times. Mean electron density has been determined under the assumption that the thickness of the loop system along the line of sight equals d in Figure 1. The horizontal bars show the e-folding radiative cooling time for the given n_e and T_e values, with conductive cooling neglected.

Figure 2 shows the *effective* loop temperature T_e, determined from the ratio of counts in the 3.5–5.5 and 5.5–8.0 keV energy bands, and the corresponding emission measure, EM. Both T_e and EM have been determined for the brightest element in the coarse field of view of HXIS $(32'' \times 32'')$ which corresponds approximately to the area within the 25% isophote in Figure 1. Thus $EM = n_e^2 Al$, where n_e is the mean electron density in a column of area $A = 32'' \times 32''$ and thickness l. One can approximate $l \simeq d$, thus assuming that the line-of-sight thickness of the inclined loop system is the same as the apparent distance of its top from the $H_\parallel = 0$ line. In that case we get the n_e values shown in the lower portion of Figure 2: Decreasing from $n_e \simeq 1.4 \times 10^{11}$ cm^{-3} at 21:11 to $n_e \simeq 1.0 \times 10^{10}$ cm^{-3} at 23:06 UT.

Since $n_e \sim l^{1/2}$, our approximation $l \simeq d$ may hardly cause errors exceeding a factor of 2. More important would be inhomogeneities in the loop structure which might involve electron condensations that we do not detect. Thus, as a matter of fact, the n_e values plotted in Figure 2 should be considered as the minimum electron densities in the loops.

When n_e is known, one can estimate the radiative cooling time of the loops. We mark the corresponding e-folding cooling times τ_r (Moore *et al.*, 1979; Raymond *et al.*, 1976) by horizontal bars in Figure 2. For example, the bar running from the n_e value at 21:11 shows that the original $T_e = 9.1 \times 10^6$ K should decrease to its $1/e$ value ($=3.4 \times 10^6$ K) at 21:23, which implies that at that time (and even some time before) those loops could not be seen any more by HXIS. Still, we see a powerful loop system at 21:23 at $T_e = 8.9 \times 10^6$ K.

This means that the existing loops must be permanently heated or, otherwise, that we see completely different loops at 21:23 than those we saw at 21:11. And the same argument is valid for any other later time as well. (Note that the n_e's in Figure 2 are the minimum values and that conductive cooling has been completely neglected.) Thus we arrive, on the basis of much more detailed observations, at the same conclusion Moore *et al.* (1979) and Petrasso *et al.* (1979) obtained for the flare of 29 July 1973: The cooling time of the flare loop system, even late in the flare, is much shorter than the time of visibility of the loops in X-rays. Therefore, there must be either a continuous release of energy in the existing loops, or new loops must be heated and become visible as time proceeds. Because we have evidence that the loops cool (we see them sequentially in cooler lines and eventually as the 'post-flare' loops in Hα), the second alternative must be the right one. Since the loop system grows, the newly seen loops must extend to larger altitudes than those that preceded them.

Because it appears difficult to find an agent which would successively excite preexisting higher and higher loops with a speed of a few km s^{-1} hours after the flare maximum, the easiest interpretation of the observed facts appears to be a successive formation of new loops above the active region. Thus, in agreement with Skylab results, our observations in the first two orbits when HXIS looked at the flare support the Kopp and Pneuman (1976) model of field opening at the flare onset, and subsequent sequential reconnection of newly formed flare loops for several hours after the flare maximum. We will see, however, that this model runs into difficulties if completely new observations, described in the next sections, are considered.

3. A Post-Flare Arch

As Figures 1 and 2 demonstrate, the flare was still very much in progress when HXIS looked last at the event, at 23:08 UT: More than two hours after the flare maximum the effective temperature was still as high as 6×10^6 K, emission measure was about 2×10^{48} cm^{-3} per one coarse element, electron density $\sim 10^{10}$ cm^{-3}, and

the loop system grew with a speed close (in projection) to 2 km s^{-1}. Thus, naturally, we were interested in the behaviour of the flare loop system also during the later orbits of the SMM, in the early hours of May 22.

Unfortunately, for the next two orbits the SMM did not look at the flare region. Thus the earliest time when HXIS could see the flare again, was at 03:08 UT on May 22. Images obtained at that time did not show in >3.5 keV X-rays any visible remnants of the flare loops in the HXIS fine field of view. However, long enough integration in the 3.5–5.5 and 5.5–8.0 keV energy ranges revealed enhanced emission in the coarse field of view, to the SSW of the flare site, i.e. approximately in the direction the loops had been growing before.

Figure 3 shows the result of a 25 min integration of the 3.5–5.5 X-ray images at that time (average time: 03:20:45 UT). The maximum count per one element of the coarse field of view (32″×32″) was 127 counts, whereas the background is 7.0 counts (4.56×10^{-3} counts per second). Thus the net maximum count was 120 per one coarse element, with 1σ-uncertainty of ±11 counts. Note that the 25% contour in Figure 3 still exceeds 4.3 times the background, with 1σ-error equal to ±1.0 times the background, so that its shape is statistically significant.

It is to be emphasized that the background per element of the fine field of view of HXIS is the same as per element in the coarse field, but the fine field counts for an extended source are expected to be lower by an order of magnitude. Thus one cannot detect any phenomena of such a low count-rate in the fine FOV, but one can do it in the coarse field as Figure 3 clearly demonstrates. (More details about the background and its variations can be found in Boelee (1982).)

In the event of 29 July 1973 the soft X-ray flare loops were seen growing, with $v \simeq 1$ km s^{-1}, still 7 hr after the flare onset (Moore *et al.*, 1979; Nolte *et al.*, 1979). Thus one might assume that we observe here a similar situation, imaging in Figure 3 the tops of the flare loops, still growing more than 6 hr after the flare beginning. However, this has proved not to be true.

If one compares the last contour plot in Figure 1 with Figure 3, the maximum emission at 03:20 UT is definitely situated too high. The d value for the maximum patch is now close to 95 000 km so that the loops would have had to grow with an average apparent speed of 4.7 km s^{-1} after 23:06 to reach the altitude observed at 03:20. This is quite incompatible with Figure 1, where the continuously decreasing apparent speed v was lower than 2 km s^{-1} at 23 UT. Also, as we shall see below, the top of the object imaged in Figure 3 did not change its height (i.e. its d value) for the following 5 hr.

Therefore, we obviously do not image here the post-flare loops, the tops of which must be situated much lower, i.e. closer to the original flare site. They are obviously no longer visible above 3.5 keV. This is understandable when one looks at Figure 2: With the emission measure rapidly decreasing (faster than in the 29 July 1973 event, cf. Švestka *et al.*, 1982a), T_e may be now (6.5 hr after the flare onset) below the critical temperature value needed for HXIS imaging. Thus we see here a completely different post-flare phenomenon, hot enough to be seen by HXIS, and
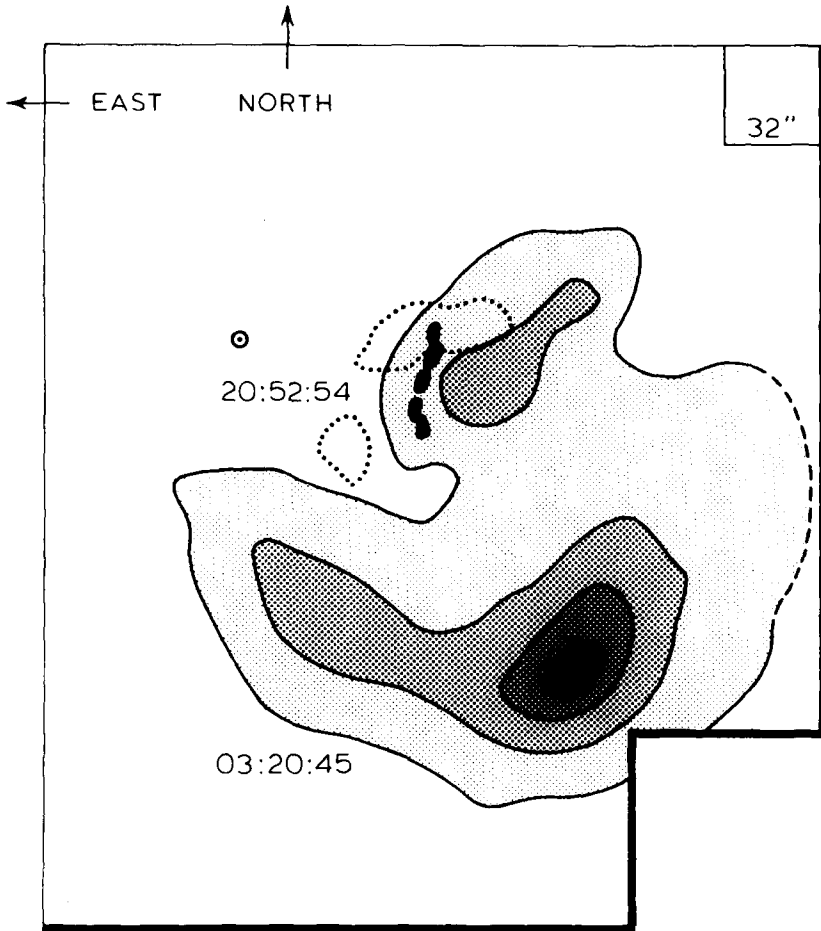
Fig. 3. The result of 25 min (1525 s) integration of 3.5–5.5 keV X-rays at the beginning of the fifth SMM orbit after the flare (mean time of integration: 03:20:45 UT on May 22). The imaged structure is almost exclusively in the coarse field of view of HXIS. (Heavy lines show the borders of the coarse field of view, center of the HXIS field of view is marked by a circle.) The contours are at 90, 75, 50, and 25% of the maximum count which was 120 (=4.7 counts per min = 0.079 counts s^{-1}) per one coarse element (32″×32″, scaled in the upper right-hand corner). For a comparison, we repeat here the first contour plot of Figure 1, at 20:52:54 UT (dotted contour, 50% of max. intensity). The black blobs are the sequential images of 90% intensity contours of the flare (the flare loop tops) at 20:57:30, 21:16:00, 21:24:00, 22:25:30, and 23:05:57 UT. (With time growing, the tops shift to the south.)

situated at a projected altitude of about 100 000 km above the flare. (This would represent a real altitude of 460 000 km for $\alpha = 0°$, i.e. without any inclination to the south.)

Figure 4 illustrates the time development of the object we image, this time as a sum of counts in the energy band from 3.5 through 8.0 keV. The background has been subtracted. For each sequence of times there are two rows of images: The upper one shows the X-ray contours for a given time, whereas the lower row
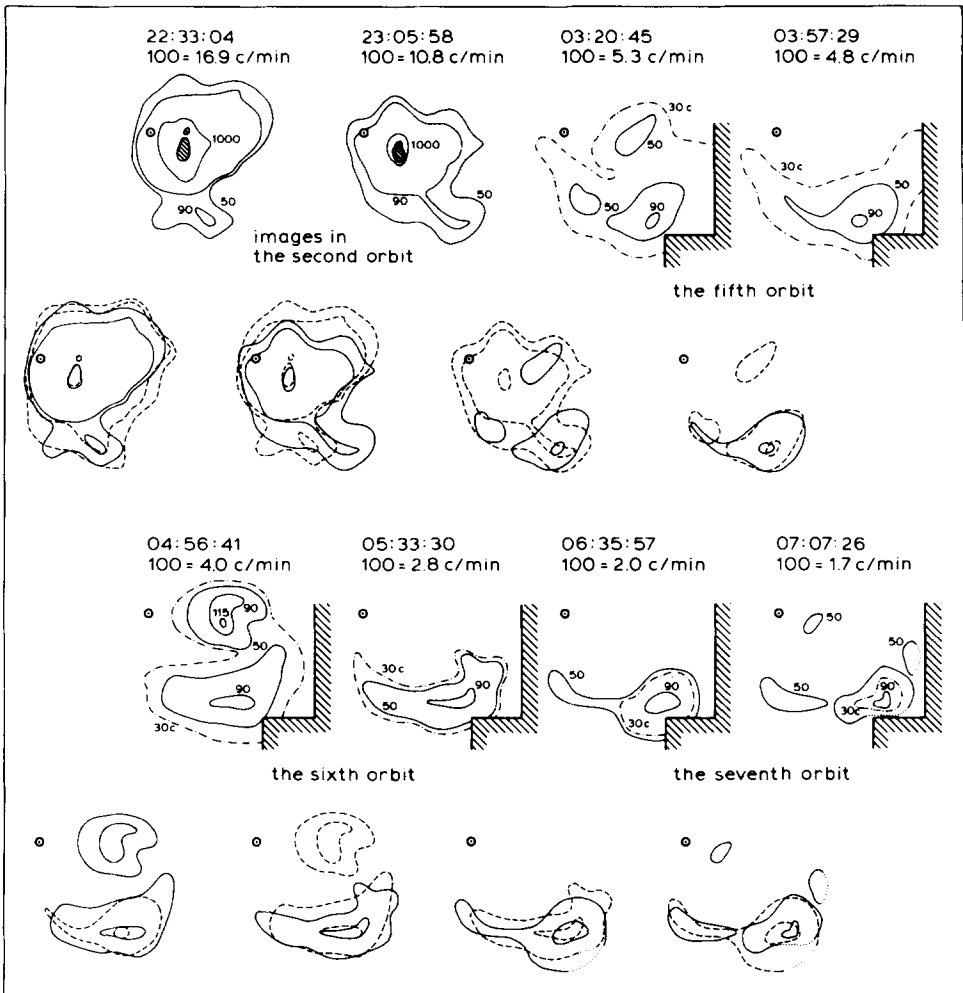
Fig. 4.   Sequence of integrated images of the structure imaged in Figure 3, in the energy range of 3.5–8.0 keV. The contours are at 90 and 50% of the maximum count rate in the structure, and this 100% count rate is given above each image in counts/min per coarse element. In the first two images, when the post-flare loops were still visible above 3.5 keV, also the 1000% contour is added. The innermost contour there is the 50% contour of the X-ray flare from Figure 1. The contour 30c shows the limit where 30 counts (i.e. 1.5 times the background noise) have been recorded. The first two images were obtained on May 21, all the others on May 22, and the given time is the mean time of all the integrated images. The integration time was 39 s for the first image, 223 s for the second one, and 1525 s for all the others. In lower rows, each image is compared with the preceding one (dashed) and the next one (solid contours).

compares adjacent images: The earlier one dashed and the later one shown as full line. One can see that the contours, each representing a different set of integrated images, yield a consistent picture of the imaged object up to 07 UT on May 22. Only the next image, at 08:05 UT (not shown in Figure 4) begins to be blurred.

We started this discussion with the first picture in the fifth SMM orbit after the flare, at 03:20:45, looking for remnants of the post-flare loops in this late orbit and finding none. Let us now reverse the question: Could the object we found at 03:20 also be seen three orbits earlier, in the second orbit after the flare? As the first two images of Figure 4 demonstrate, it could. At 23:05:58 we see a tongue extending from the flare region to the SW which exactly coincides with the maximum of X-ray emission at 03:20.

The flare was still visible at that time. The contour 1000 marks the region within which the counts per coarse element exceeded 10 times the maximum count in the object studied. The innermost contour represents then the 50% contour of Figure 1, i.e. the top of the flare loops at that time. It is, maybe, unneccessary to note that this is another evidence that the object we see has nothing in common with the post-flare loops: Here, at 22:23 and 23:06, we see both these phenomena at the same time, and at a very reasonable distance one from the other.

The first time we can see an indication of the object of our study is at the beginning of the second orbit, at 22:25 UT, when the contours became slightly deformed towards SW. We do not show this contour plot in the first row of Figure 4, but we compare it (dashed contours) with the image at 22:33 in the second row. Thus the object above the flare, we are speaking about, was visible in 3.5–8.0 keV X-rays from ≤22:25 UT on May 21 through ~08 UT on May 22.

A look at Figure 3 and several of the plots in Figure 4 indicates strongly that we have imaged here an extensive arch, with maximum brightness at the top, at $d \simeq 10^5$ km, and foot points near the flare site. A comparison of the 90% contours in the sequential plots of Figure 4 shows that the position of the top did not change from 03:20 through 07 UT, and it possibly stayed at constant altitude since its beginning on May 21 (compare the 23:06 and 03:20 plots). On the other hand, the legs might indicate an expansion in both directions, toward NW as well as toward SE. With lower counts along the legs, however, one cannot be quite sure about the reality of this indicated motion.

Figure 5 shows the X-ray image of 03:20 superposed on the Hα image of the active region prior to the flare. As it appears, the long-integrated image represents an arch with legs rooted at both sides of the disrupted dark filament. This implies that the field lines of this arch (like those of the filament before) are generally perpendicular to the magnetic field lines in the flare loops, extending like an enormous bridge above them. The existence of such a stationary arch, with field orientation along the $H_\parallel = 0$ line, poses a problem for the Kopp and Pneuman (1976) model of the post-flare loops, as we will discuss more in detail in Section 7.

One has to realize, however, that the spatial resolution of the HXIS coarse field of view, 32″, is relatively low and that a part of the imaged structure extended out of the HXIS field of view (cf. Figure 4 and the dashed contour in Figures 3 and 5). Therefore, it is fair to say that we cannot be *absolutely* sure that our interpretation of Figure 5 is quite correct. We might have missed the real western footpoint situated out of the field of view, more to the west. The region near the western
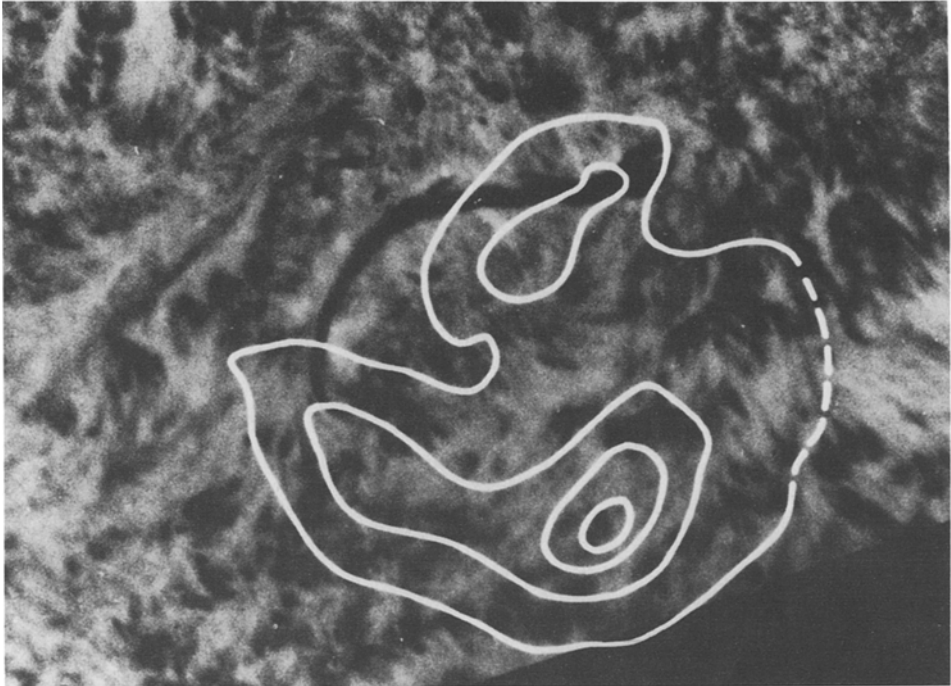
Fig. 5.   The arch of Figure 3 (at 03:21 UT on May 22) in projection on an Hα picture of the active region prior to the flare on May 21. The arch apparently connects the two ends of the (later disappeared) filament and extends along the $H_\parallel = 0$ line high in the corona. There is a slight uncertainty in alignment in the east–west direction (i.e. along the filament), because of a sudden rise in temperature on HXIS two days before the flare. This temperature variation eventually changed the HXIS pointing by 20″ to the west, but the exact time when HXIS responded to the temperature jump is not known. The uncertainty is about 1.5 degrees in the heliographic longitude.

end of the filament, which we believe to be the western footpoint, might than be a third (middle) footpoint of a double arch, or even a smaller bipolar structure below the big arch, representing perhaps late remnants of the flare. However, as Figure 3 demonstrates, this region was shifted more to the west and certainly was not in the position where the late flare-loop tops would be expected. Besides, this enhanced region could be seen by the FCS experiment aboard the SMM in O VIII and Mg XI lines as early as 17:40 UT on May 21, and the western end of the filament, with which it coincides, showed enhanced motions for hours before the flare (Gaizauskas, 1981). Thus this supposed western footpoint cannot be interpreted as a remnant of the flare and seems to have been related to the western filament leg since the preflare period.

4. Comparison with Radio Bursts

Figure 6 shows the position of the imaged hard X-ray arch on the solar disk in comparison with a post-flare stationary radio burst observed at Culgoora at 160,
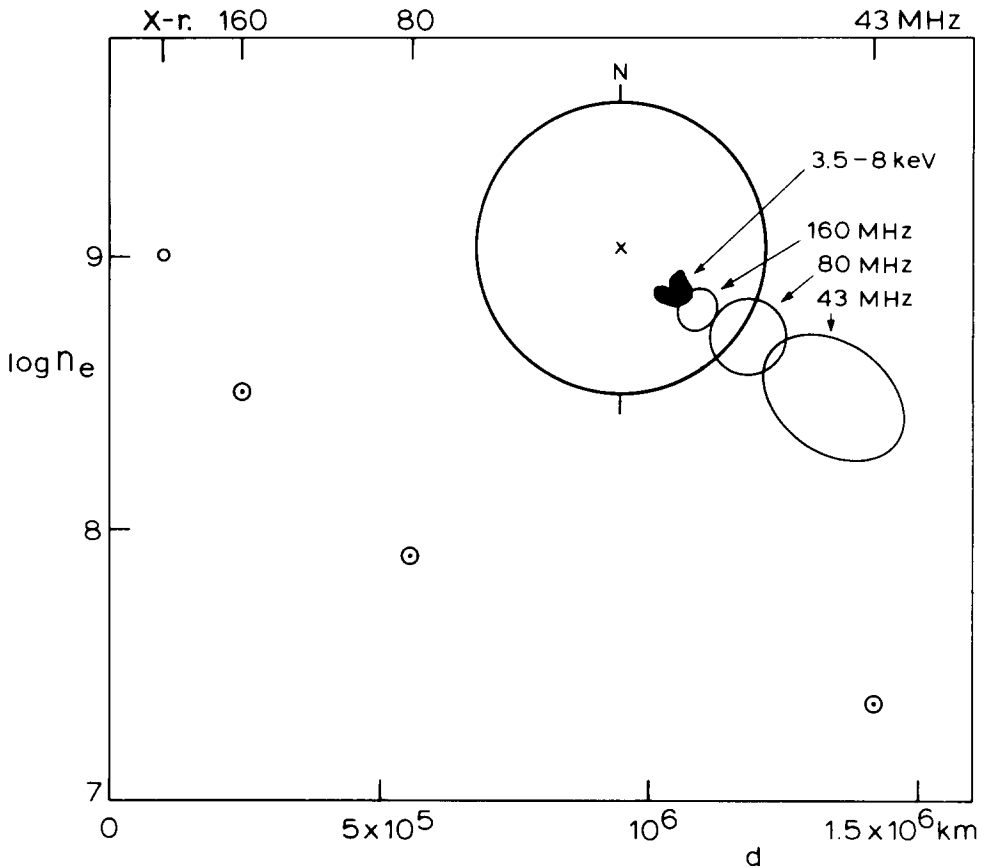
Fig. 6. The insert shows the relative positions of the X-ray arch (from Figure 5) and three images of the stationary type I noise storm as seen at Culgoora at 03:20 UT on May 22. Contours of brightness temperature for the RH-polarized component are shown for frequencies of 160 and 180 MHz, while a combined RH+LH picture is used at 43 MHz. The graph shows the n_e values obtained from corresponding plasma frequencies for the radio images, and from the emission measure for the X-ray source, in dependence on the projected distance d from the flare site.

80, and 43 MHz. This comparison clearly suggests that the arch we see in X-rays images the lowest part of an extensive magnetic bottle in which trapped accelerated electrons produce the stationary radio burst. Let us discuss in detail several facts that support this conclusion.

A. POSITION

As Figure 6 demonstrates, the X-ray arch position towards SSW above the flare coincides with the extension of the radio burst into the corona. In Table I we give the values of the projected distance from the original flare site, d, for our X-ray arch and for the various Culgoora radio frequencies.

TABLE I

d, h, h' and electron density values at 03:20 UT on May 22, 1980

Energy or frequency	3.5–8.0 keV	160 MHz	80 MHz	43 MHz
$d(10^3 \text{ km})$	95	152	380	722
$n_0 (\text{cm}^{-3})$	1×10^9	3×10^8	8×10^7	2×10^7
$h = h'$ for $\alpha = 0°$ (10^3 km)	456	731	1828	3473
$h'(h)$ for $\alpha = 20°$ (10^3 km)	171 (179)	274 (287)	695 (717)	1334 (1362)
n_0/n for $\alpha = 20°$	17	11	24	42
$h'(h)$ for $\alpha = 45°$ (10^3 km)	85 (113)	138 (181)	370 (453)	743 (861)
n_0/n for $\alpha = 45°$	7.4	3.8	5.4	7.3

Notes:
  d = projected distance of the source from the $H_{\parallel} = 0$ line (from Figure 6).
  h = real distance of the source from the $H_{\parallel} = 0$ line
        for a given α ($h = d/\cos(78° - \alpha)$).
 h' = vertical distance of the source above the solar surface.
 n_0 = electron density deduced from observations (cf. Section 4C).
  n = electron density expected in the quiet corona at the altitude h.

The radio source also indicates an inclination from the radial direction towards the south, as the flare itself did before. As we describe in Section 4C, we can estimate the electron densities n_0 in the X-ray and radio sources – they are given in the third line of Table I. If the burst extension were radial, the real altitudes h would be those shown in Table I for the $\alpha = 0°$ case. However, in that case the n_0 values exceed by a factor of 100 to 400 the electron densities n expected on those altitudes in the quiet solar atmosphere (Allen, 1973). If, on the other hand, the sources were inclined 45° to the radial, the ratio n_0/n would decrease to 3 to 8 which seem to be more reasonable values for an active region (cf. Table I).

Thus one expects a significant deviation from the radial direction to the south, for the trajectory of the eruptive filament, for the flare loops, for the X-ray arch, and for the radio source. The exact angle α of this inclination is still unknown, because we do not know the real electron density distribution in the corona above the flare. Another way to estimate it is to look at the inclination of structures observed when the active region crossed the west limb. The SMM coronagraph images indicate a southward tilt of roughly 20° from the vertical. Therefore, we have added also the altitude and density values for $\alpha = 20°$ to Table I. One can suppose that the real values are between those given for $\alpha = 20°$ and 45°, respectively. The radio heights thus attained are consistent with type I sources observed on the solar limb (Stewart, 1976).

In agreement with the completely stationary shape of the X-ray arch, the radio source also remained stationary during Culgoora observing times from 23:16 to 05:10 UT, i.e. for 6 hr. Hence whatever magnetic configuration and density structure confined the X-ray and radio-source regions these structures remained remarkably constant for 6 to 8 hr after the flare.

B. TIME DEVELOPMENT

The radio spectrograph at Culgoora observed a type II burst associated with the flare, starting at 20:57 UT on May 21, and lasting until 21:27 UT. Perhaps since 21:10 UT, and definitely since 21:30, a type IV burst was observed at 20–200 MHz. We assume that the burst was stationary, but have no position observations until 23:16 when the heliograph started to observe. It was stationary for at least six hours after that. The burst was at first a mixture of continuum and type I noise storm, but it could be classified as pure type I noise storm after 23:50 UT. The spectrograph could follow this storm until 02:45 on May 22; weak revivals of the storm, in the range of 50–70 MHz, could be still recognized until at least 06:40 UT. The Culgoora heliograph started to observe at 23:16 UT and could follow the noise storm until the end of the observing period at 05:10 UT on May 22.

These times agree well with the X-ray data: We can identify the burst in X-rays since the beginning of the second orbit, at 22:25 UT. We were unable to recognize the source in the first orbit, because of the high X-ray background due to the flare itself at that time. Later on, we could image the bottom of the burst all the time Culgoora saw it with the heliograph, and about two hours more after the end of their observing period. Figure 7 compares the brightness temperatures of the radio source at 160 and 80 MHz with the maximum counts at the top of the X-ray arch. One can clearly see that the behaviour during the decay was quite similar.

It follows that we have imaged the stationary component of a type IV burst after it was transformed into continuum and later on into regular post-flare type I noise
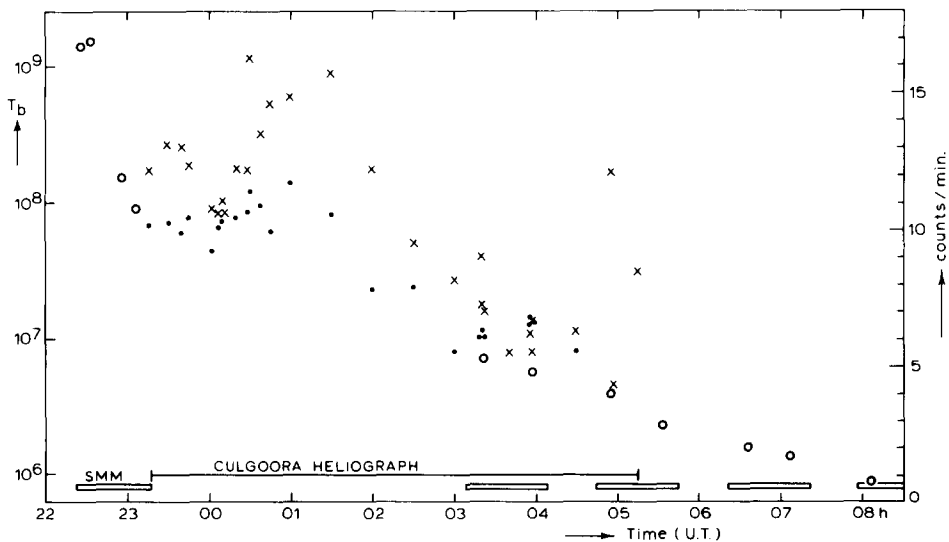

Fig. 7.   Maximum brightness temperatures of the type I noise storm radio source imaged by the Culgoora spectroheliograph at 160 MHz (dots) and 80 MHz (crosses), compared with the maximum count rates (per one pixel of the coarse field of view, right-hand scale) in the 3.5–8.0 keV images of the X-ray arch (circles). The observing times aboard the SMM and at Culgoora are shown at the bottom.

storm. Such a transformation of type IV is commonly observed after two-ribbon flares (see, e.g., Švestka, 1976), and Webb and Kundu (1978) have reported type I noise storms initiated by filament eruptions even without Hα flares.

C. ELECTRON DENSITY

At 03:20 UT the maximum count rate in the X-ray arch, per 1525 s and one coarse element, was 127 in the energy band 3.5–5.5 keV and 27 in the band 5.5–8.0 keV. After subtracting the backgrounds, we find an effective temperature from the ratio of these two energy bands equal to 6.5×10^6 K, with 1σ-deviation limits of 6.2 and 7.0×10^6 K. The corresponding emission measure per one coarse element is 7.2×10^{46} cm^{-3}. Then the mean electron density in the arch is $1.0 \times 10^{14} \, l^{1/2}$ cm^{-3}, where l is the geometrical thickness of the arch along the line of sight.

One can suppose 10^4 km $\ll l \lesssim 10^5$ km $(=d)$. For these limits one gets 1.0×10^9 cm$^{-3} \lesssim n_e \ll 3.3 \times 10^9$ cm^{-3}. Thus a value close to 10^9 cm^{-3} seems to be a reasonable estimate for the mean electron density in the X-ray arch. (Provided that the emission is thermal; we will see in Section 6 that this really appears to be the case.)

On the other hand, the radio emission becomes visible at the fundamental plasma frequency level in the corona which corresponds to

$$n_e^{1/2} = (\nu/9) \times 10^3 \text{ cm}^{-3},$$

with ν in MHz. These densities have been shown in Table I (n_0), and they are also plotted, for the corresponding distances d from the flare at 03:20, in the graph of Figure 6, being compared there with the density deduced from the X-ray images. The figure proves a smooth run in density throughout the magnetic bottle as one would expect with the X-ray arch being a bottom part of it.

5. Time Variability of the Source

As one can see from Figure 7, the radio source greatly varied in brightness, whereas the X-ray source was decaying smoothly, without any drastic temporary changes in brightness. However, this was true only for the top portion of the X-ray arch, while the visibility of the footpoints varied greatly. One can see it clearly in Figure 4, where both the footpoints were visible at 03:20, but only the eastern one appears at 03:57, and only the western one at 04:56. At the latter time the western footpoint, completely invisible before, was brighter than the top of the arch.

Figure 8 shows at its bottom the time variation of the five brightest coarse-field elements near the arch top (solid line) and near the western footpoint (dashed line). A five-minute integration time has been used throughout. One can clearly see that while the count variations at the top do not exceed ±20%, there are striking variations in the counts at the footpoint during the orbit 03:16–04:15 UT and, in particular, at the beginning of the orbit 04:44–05:42.
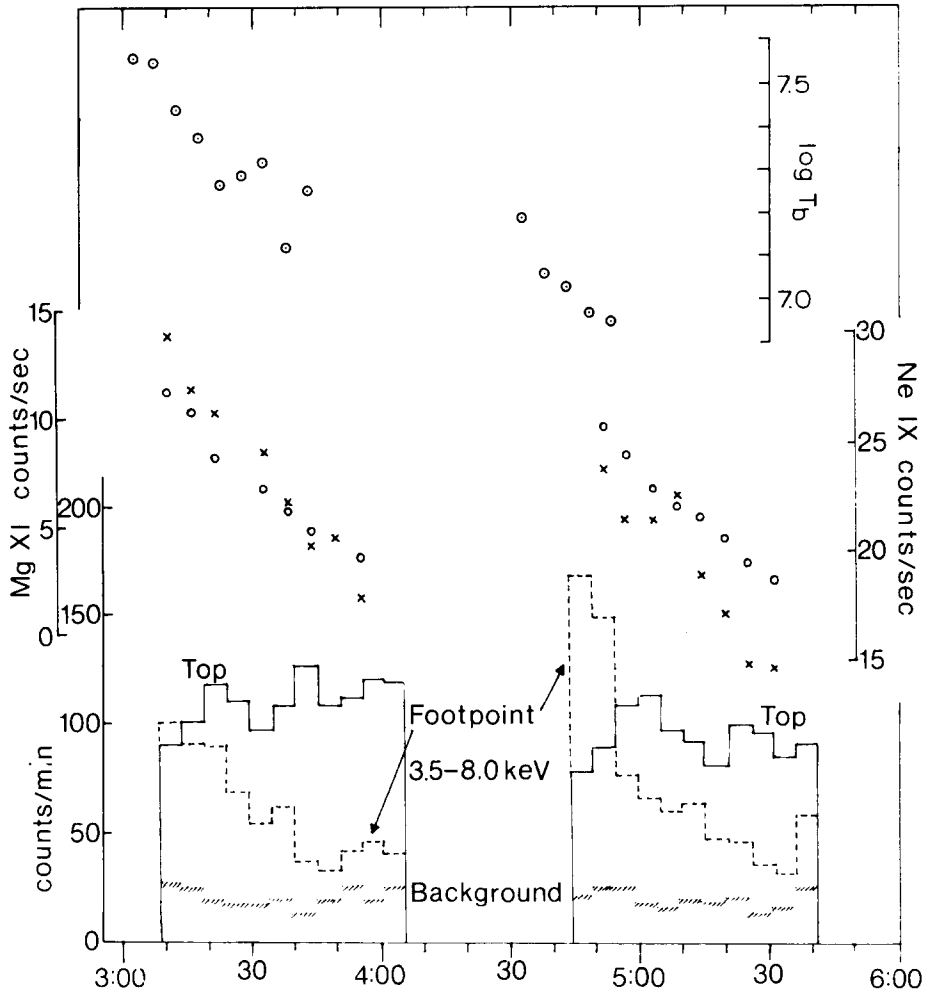
Fig. 8. At the bottom we show the time variation (in counts per min) of the five brightest coarse field elements near the arch top (solid line) and near the western footpoint (dashed line), by using five-minute integrations. At the top we compare it with time variations of the maximum brightness temperature at 80 MHz. In the middle we show FCS count rates for Mg XI (circles) and Ne IX lines (crosses) near the western footpoint of the arch. Unfortunately, no reliable T_b data are available from Culgoora for the second orbit.

The top of the arch could be seen all the time clearly in the 3.5–5.5 keV band, and weakly in the energy range of 5.5–8.0 keV. It was never visible above 8.0 keV, as Table II demonstrates. In contrast to that, the western footpoint was often very weak even in the 3.5–5.5 keV band, but as soon as it brightened, it became visible also at energies above 8.0 keV. As Table II shows, the footpoint count rate in the 8.0–11.0 keV channel of HXIS was distinctly above the noise level at 03:20:45 (±12.7 min) and 04:56:41 (±12.7 min), when the 3.5–8.0 intensity of the

TABLE II

Counts in the 8.0–11.0 keV band

Mean time (22 May)	Integration time (s)	Counts (±1σ deviation)	
		Top	West. footpoint
03:20:45	1525	0.8±4.3	9.8±4.7
03:57:29	1525	−1.2±4.2	2.0±4.4
04:56:41	1525	0.0±4.3	18.1±5.0
04:48:42	610	0.4±6.8	21.0±8.1

footpoint shows the maxima in Figure 8. The count rate is still higher when we restrict the integration time to 10 min at the time of the pronounced maximum at 04:48:42 (±5.1 min) in Figure 8. Thus the footpoint, when visible, shows definitely a harder energy spectrum in X-rays than the top of the arch.

Therefore, one can conclude that the footpoints of the observed X-ray arch manifest great variability in their intensity and in the hardness of their spectra, while at the same time conditions in the top of the arch remain apparently unchanged. We will see in the next section that the X-ray arch was basically thermal, and its temperature stayed rather constant. In contrast to that, the radio noise region above was highly variable in brightness, it was clearly nonthermal, and it was an intermittent source of particle acceleration producing bursts of radio noise as it is commonly observed in type I noise storms. Thus the brightenings near the footpoints of the arch may be due to occurrences of transient bursts of accelerated particles which dump electron streams into the low corona and transition layer.

If this is the case, then the acceleration is probably accomplished outside the X-ray arch, much higher in the corona, as the top of the X-ray arch did not vary in brightness. In a magnetic bottle above an active region (cf. the schematic drawing in Figure 9) the footpoints of high-extending field-lines need not be far from each other. Thus particles dumped from the radio burst regions can excite the low corona close to the point we image in X-rays, and the difference in position might not be recognized within the spatial resolution of HXIS coarse field of view.

In such a case, we may expect a correlation between time variations in the radio brightness high in the corona and X-ray counts near the footpoints. Unfortunately, a comparison of these two sets of data is complicated by the lack of overlap in time between the Culgoora and HXIS data. As Figure 8 shows, the 80 MHz brightness temperature T_b was decreasing after 3:00 UT and prior to 5:00 UT, in apparent correlation with the X-ray counts at the western footpoint. T_b at 160 MHz (lower in the corona) did not show these variations. However, there are no reliable radio data shortly before and after 5:00 UT when the most striking X-ray variation occurred. T_b was then steeply decreasing at both radio frequencies, but at the same time the radio beam was leaving the Sun and we are unable to say how much of the flux decrease was due to this effect. Therefore, the only conclusion we can draw
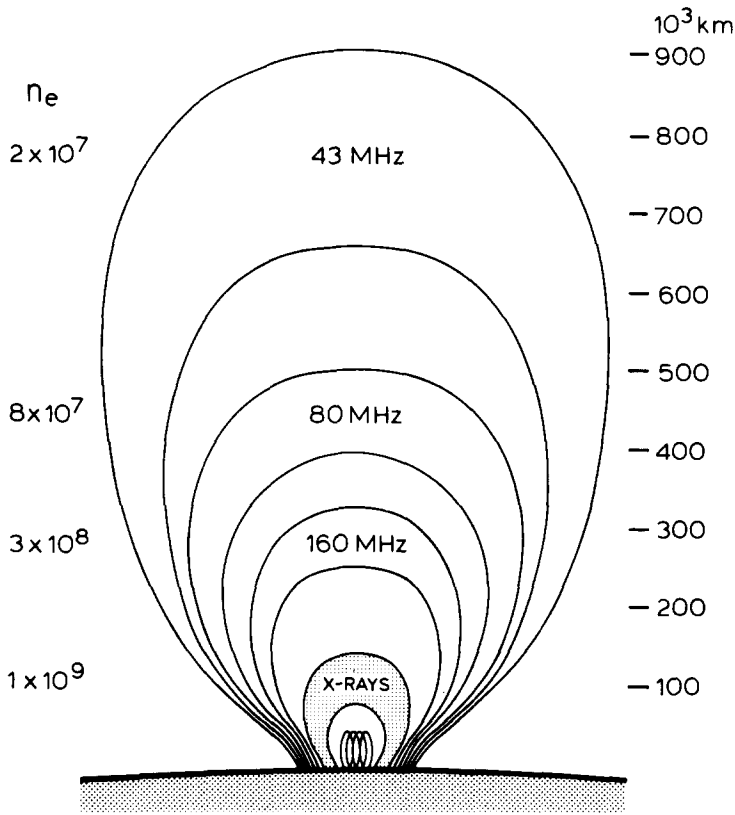
Fig. 9. A schematic drawing of the magnetic bottle at the bottom of which we observe the X-ray arch. The numbers to the left give the approximate electron densities at which the various radio frequencies and the X-rays are emitted. The right-hand scale gives the altitudes of the various emissions in projection on the solar disk. If the bottle extended radially above the flare, this scale is to be multiplied by a factor of 4.8. In reality, the bottle was probably inclined to the south so that the multiplying factor is smaller (1.1–1.9 are the most likely values).

is that there *may be* a correlation between the 80 MHz T_b values and X-ray counts near the western footpoint, but more data (for other post-flare arches) would be needed to prove it (cf. Švestka *et al.*, 1982b).

Other SMM experiments that can image the Sun are the flat crystal spectrometer (FCS, Acton *et al.*, 1980) and the ultraviolet spectrometer (UVSP, Woodgate *et al.*, 1980). They could not see the top of the arch, because it was out of their fields of view, but they might have imaged the western footpoint. The UVSP pictures, made in low-temperature hydrogen Lα (1215 Å) and C IV (1548 Å) lines, show the chromospheric and transition-layer post flare plage in the active region, and this structure masks any small brightness variations that might possibly occur at the site of the footpoint deep in the atmosphere (below $\sim 10^5$ K). At higher temperatures, in the FCS lines (above 2×10^6 K), the count-rate light curves for

the region suspected to be the footpoint show time variations nicely correlating with those found from HXIS and Culgoora data in Figure 8. As examples, we present in the middle part of Figure 8 the count-rate curves for Mg XI at 9.17 Å (corresponding to $\sim 6 \times 10^6$ K) and Ne IX at 13.45 Å ($\sim 3.5 \times 10^6$ K).

We intend to study more in detail the time variations in the radio and X-ray emitting regions, and their impact upon lower atmospheric layers in a separate paper.

6. The Physical Nature of the Arch

Because of the low counts and high background, especially above 5.5 keV, any determination of the effective temperature, deduced from the count ratios in the 3.5–5.5 and 5.5–8.0 energy bands, involves large errors. Nevertheless, as Table III shows, the effective temperature at the top of the arch can be safely established to be close to 6.5×10^6 K and, surprisingly, this value does not seem to decrease in any significant way during the whole period of our observations, from 23 UT on May 21 through 06 UT on May 22.

We can also get temperature data from the bent crystal spectrometer on the SMM (BCS, Acton et al., 1980). This instrument yields an X-ray spectrum of the entire arch, including footpoints. Because of the faintness of the source only the Ca XIX channel (3.165–3.321 Å) produced useable spectra. Examples of BCS spectra and their analysis are given by Culhane et al. (1981) and Gabriel et al. (1981).

As BCS and the HXIS bands 1 and 2 respond to the same range of plasma temperatures, the HXIS images unambiguously identify the source region of the BCS spectra. Theoretical fits to the BCS spectra, taking account of Ca XVIII satellite lines excited by dielectronic recombination and inner shell transitions yield electron temperatures and information on the ionization state of the plasma. The electron temperatures and Ca XVIII/Ca XIX (Li-like/He-like) abundance ratios so derived are given in Table III. Reference to the 'top' and 'footpoint' rates shown in Figure 8 establishes that for the 03:53:59 and 05:19:37 data sets the arch top emission predominates. In this temperature range the Ca XIX satellite to resonance line ratio is a very sensitive thermometer and these mean temperatures are judged to be reliable. They corroborate the HXIS filter ratio results which are essentially a continuum measurement and this agreement between two independent measurements gives evidence for the thermal nature of the X-ray emission from the arch.

Because of the statistical weakness of the BCS data the Li/He ratios are poorly determined but seem to be in agreement with expectations for an equilibrium plasma (compare the measured and the bracketed values in Table III). Only in the case of the 4:47 UT footpoint burst (with Li/He $\simeq 2.0$) the observed ratio is significantly higher than the expected one. This may indicate a possibility of suprathermal electrons contributing to the line excitation, as we suggested in the preceding section. At that time also the hardness of the footpoint spectrum increased (cf. Table II).

TABLE III

Values of temperature, emission measure, and Li/He ratio in the arch

Mean time (UT)	Integration time	T_e(HXIS) (10^6 K)[a]		T_e (BCS) (10^6 K)	Li/He[b]	Emission measure (cm^{-3})	
		1 element	5 elements			1 element	Total
23:05:58 (21st)	223 s	$6.4^{6.1}_{7.7}$				1.65×10^{47}	
03:20:45 (22nd)	1525 s	$6.5^{6.2}_{7.0}$	$6.2^{6.1}_{6.6}$			7.2×10^{46}	1.12×10^{48}
03:25:05	1791 s			7.0 ± 0.5	1.20 (0.91)		
03:53:09	1678 s			6.0 ± 0.5	1.50 (1.48)		
03:57:29	1525 s	$6.3^{6.0}_{7.1}$	$6.2^{6.1}_{6.6}$	6.4 ± 0.5	2.00 (1.20)	8.0×10^{46}	9.5×10^{47}
04:49:47	563 s						
04:56:41	1525 s	$6.6^{6.3}_{7.4}$	$6.1^{6.0}_{6.7}$	6.4 ± 0.5	1.00 (1.20)	4.7×10^{46}	8.1×10^{47}
05:19:37	2951 s						
05:33:30	1525 s		$6.7^{6.5}_{7.1}$				
05:46:48	1525 s	$6.4^{6.1}_{8.4}$				4.3×10^{46}	
06:35:47	1220 s		$6.2^{5.9}_{\infty}$				

[a] At the top region of the arch, with ±1σ deviation limits.

[b] Theoretical values, expected in an equilibrium plasma, are in brackets (after Doyle and Raymond, 1981).

However, also the equilibrium values of Li/He, observed at all the other times, do not exclude an admixture of non-thermal electrons in the arch, because the thermalization time for the arch density is quite short (cf. Table IV). It is thus possible that some of the high-energy electrons which dump upon the low corona near the footpoints are mirrored upwards, but instead of going back along their original trajectories they drift into the X-ray arch region, are trapped there, and may contribute to the arch heating. This trapping of dumping energetic particles may be a permanent phenomenon (temporarily enhanced during the visible brightenings of the footpoints) which represents a continuous supply of energy for the arch.

TABLE IV

Collisonal loss times, τ_c, of suprathermal electrons (after Brown, 1971) in regions with ambient density 1×10^9 cm^{-3} (the X-ray arch), 3×10^8 cm^{-3} (160 MHz radio source), and 2×10^7 cm^{-3} (43 MHz source)

n_e / Energy	1×10^9 cm^{-3}	3×10^8 cm^{-3}	2×10^7 cm^{-3}
30 keV	25^s	1^m 22^s	20^m 32^s
100 keV	2^m 30^s	8^m 20^s	2^h 05^m
300 keV	25^m 30^s	1^h 25^m	21^h 15^m

Table III also gives the mean values of the emission measure corresponding to the mean temperature for 1 coarse element. This emission measure per coarse element was continuously decreasing, indicating a decrease in electron density (by about factor 4 from 23 UT on May 21 through 06 UT May 22). The total emission measure of the whole cloud could be determined for three images only: It decreased from 1.2×10^{48} cm^{-3} at 03:21 to 7.1×10^{47} cm^{-3} at 04:57 UT. With a density of 10^9 cm^{-3} at 03:21 the total volume of the arch would be 1×10^{30} cm^3. One could model it, e.g., by a semi-circle arch of 60 000 km thickness extending from 70 000 to 130 000 km above the surface of the Sun. At 03:21 UT the whole arch emitted 326 photons cm^{-2} s^{-2} above 3.5 keV.

7. Consequences for Flare Models

According to the Kopp and Pneuman (1976) model of post-flare loops, which can be considered as a general model of two-ribbon flares (Švestka *et al.*, 1980; Pneuman, 1981), the magnetic field opens as the filament erupts, and it subsequently closes again through reconnection driven by the prevalence of magnetic pressure over gas pressure. The reconnection starts low in the atmosphere and proceeds upwards with decreasing speed.

Each process of reconnection produces two loops: One, rooted in the photosphere, is seen as the (post-) flare loop in X-rays and later on, after it cools, in

H$\overset{\cdot}{\alpha}$; the other is opened upwards (eventually being closed at much higher altitude) and is expected to rise into the corona and to contribute to the creation of a coronal transient. According to Anzer and Pneuman (1982) these upper disconnected loops produced through reconnection provide the driving force for the transient.

Now, we have imaged a stationary arch that appears to extend along the $H_\parallel = 0$ line above these reconnection sites. Thus, the upper disconnected loops cannot move upwards and instead should wind up around the arch-like magnetic bottle above the flare.

We do not know, of course, whether the arch existed from the beginning of the flare. Culgoora began to see the mixture of continuum and type I spikes at 21:10 UT, and HXIS established the existence of the arch first at 22:25 UT. Thus, the upper disconnected loops could produce the transient in the early phase of the flare, but its formation had to be finished at 21:10 (about fifteen minutes after the filament eruption), or, in the extreme case, prior to 22:25, when the arch was clearly present.

As a matter of fact, we have no definite evidence that the basic configuration of the arch are field lines running along the $H_\parallel = 0$ line; the arch could be also composed of loops oriented across the $H_\parallel = 0$ line like the flare loops are. But this evidently does not make the theoretical interpretation any easier, since we would have then two separate systems of loops crossing the $H_\parallel = 0$ line at two different altitudes. The field lines in the Kopp and Pneuman model cannot reconnect twice.

Thus one can believe, indeed, that the magnetic field in the arch is interconnected in the direction perpendicular to the plane of the flare loops, as the filament was, prior to the flare. It might be (as C. J. Durrant suggested in a private discussion) that only a part of the original filament erupts high into the corona, whereas its remnants escape the driving force during the rise and stay stabilized at some altitude in the corona. Indeed, as A. Bruzek (in private communication) has emphasized, the mass of the X-ray arch (10^9 particles $\times 10^{30}$ cm$^3 \times 10^{-24}$ g = 10^{15} g) is close to the total mass of a quiescent filament. In such a case, the arch would exist since the onset of the flare, and the Kopp and Pneuman (1976) and Anzer and Pneuman (1982) models of the formation of coronal transients could not work. The only way to remove this obstacle is to assume that the flare loops and the post-flare arch had greatly different inclinations, but this has not been indicated by the observations.

However, a field-line interconnection perpendicular to the plane of the flare loops can be formed also by the Kopp and Pneuman process itself, as we have tried to show schematically in Figure 10: Anzer and Pneuman have drawn attention to the fact that the field lines prior to the flare are greatly sheared. Thus, after they open there is no apparent reason why the field lines would reconnect with themselves. Rather, in order to simplify the magnetic configuration, reconnection is most likely to take place between the nearest disconnected field lines. Yet, the field lines do not actually open, they just extend far into the corona but remain closed. Therefore, the reconnection with a neighbour field line means for the upper
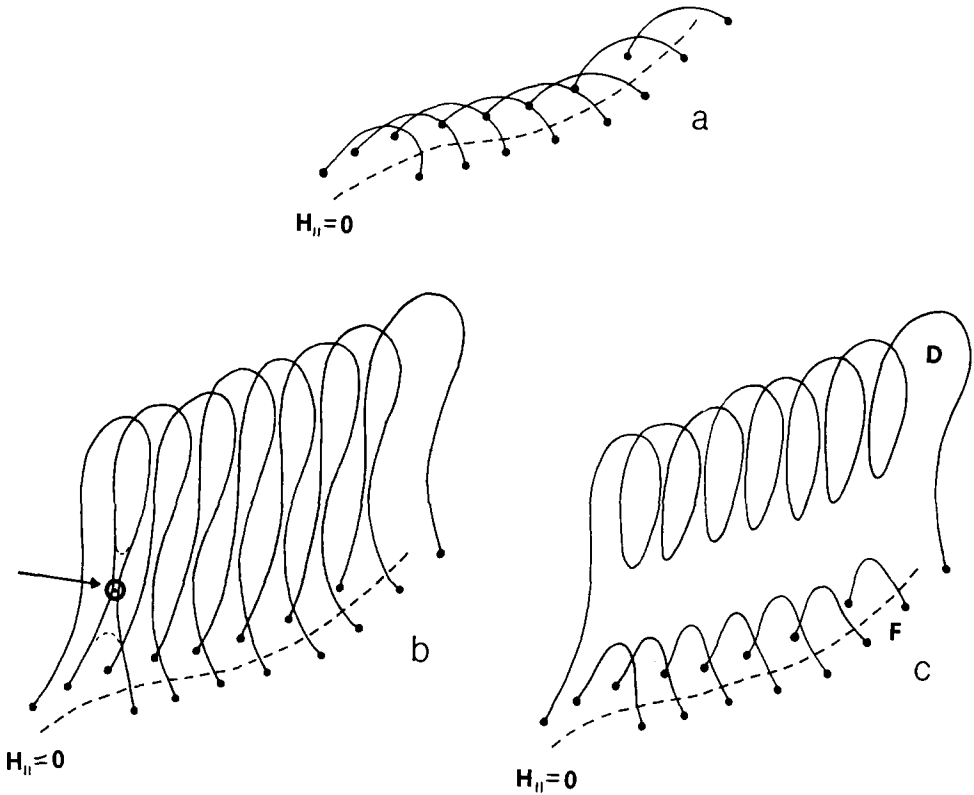
Fig. 10.   If the magnetic field is sheared (a), and is extended upwards during the filament eruption (which looks like field-opening at lower levels, (b)), reconnection may occur between neighbouring field-lines (arrow in (b)). As a result we get then less sheared flare loops below (F in (c)), while the upper disconnected loops (D in (c)) are topologically interconnected along the $H_\parallel = 0$ line.

set of disconnected loops the formation of a system topologically interconnected along the $H_\parallel = 0$ line, similar to the magnetic arch (bottle) which Culgoora and HXIS imaged above the decaying flare.

However, in Anzer and Pneuman's picture these sequentially reconnected field systems (arches) move steadily upwards, driven by magnetic pressure from below. Presently we do not see how to reconcile this model with the existence of the stationary arch we see, unless the moving coronal arch (i.e. the coronal transient) eventually becomes detached from the solar surface as an isolated blob, and leaves behind a reconnected stationary system of further reconnecting loops (Figure 10) which does not move upwards anymore, because the driving force of the continuing reconnection processes is now too small.

As Švestka *et al.* (1980) have shown, each process of reconnection of the post-flare loops might produce accelerated particles. Although the production of accelerated particles late in the flare process must be small and inefficient, the

continuing reconnection may still inject some ~10 keV particles into the system of the upper reconnected loops. Because of the interconnection of the neighbouring field lines (Figure 10) these particles are trapped in the arch and get thermalized. Thus they might provide another continuous source of energy contributing to keep the arch at more or less constant temperature as long as the flare reconnection process below continues. One may mention here that Kuperus and Van Tend (1981) propose a model in which post-flare loops are formed without a topological need for reconnection; nonetheless reconnection could provide accelerated particles also in this case.

8. Summary

HXIS imaged the two-ribbon flare of 21 May 1980 from its onset at 20:50 through 23:17 UT, except the satellite night from 21:35 to 22:21. During that time the effective temperature of the flare loops in the 3.6–8.0 keV energy range decreased from $>11 \times 10^6$ K to 6×10^6 K, and the averaged electron density varied from $>1.5 \times 10^{11}$ cm^{-3} to 1.0×10^{10} cm^{-3}. For these electron densities the radiative cooling time is much faster than the observed lifetime of the flare. Therefore, energy must have been released continuously in the flare during the whole time of HXIS observation, most likely by forming new flare loops at successively higher altitudes. The growth of the loop system (in projection on the disk) was about 30 km s^{-1} in the onset phase, and the loops still grew with a speed of ~2 km s^{-1} at the end of HXIS observations after 23 UT.

For the following two orbits the SMM did not look at the flare region, coming back to it only at 03:08 UT on May 22, more than six hours after the flare onset. At that time the flare loops were not visible any longer above 3.5 keV, although the 'two-ribbon' footpoints were still evident in the FCS and UVSP images corresponding to lower temperatures. The loop temperature evidently was below the threshold level of HXIS imaging. Instead, however, HXIS imaged an arch which extended along the $H_{\parallel} = 0$ line to a projected distance of ~100 000 km above the flare, about 2.5 times higher than the flare loops should have been at that time. If the arch extended in a radial direction above the flare, its real altitude would be 460 000 km, but it was probably inclined to the south and thus lower (110 000–180 000 km is the most likely range of its altitude). ·

The top of the arch could be first recognized at the beginning of the second SMM orbit after the flare, at 22:25 UT on May 21, and it could be imaged with good enough count-rate statistics until 07 UT on May 22. All this time the top did not change its altitude, nor its effective (3.5–8.0 keV) temperature which remained close to 6.5×10^6 K, but its brightness in >3.5 keV X-rays was decreasing with time, in consequence of decreasing emission measure. This decrease was steady, without any abrupt brightness variations.

In contrast to that the supposed footpoints of the arch were greatly variable in brightness and in the hardness of the emitted radiation. During short periods of

enhanced brightness the western footpoint could be imaged also above 8.0 keV, where the top was permanently invisible; at other times this footpoint could be hardly recognized even in the 3.5–5.5 keV band. These variations could be seen also in several FCS lines. The BCS spectra taken aboard the SMM give an evidence that the arch emission was basically thermal, possibly with an admixture of non-thermal radiation in particular at the times when the footpoint brightened. The deduced mean electron density of 10^9 cm^{-3} in the arch is consistent with thermal nature of the arch radiation, because in plasma of that density even 100 keV electrons are thermalized within a few minutes.

A comparison with radio observations at Culgoora reveals that the X-ray arch was the bottom part of an extensive magnetic bottle above the flare, in which trapped accelerated suprathermal particles produced for many hours a stationary post-flare burst. A continuum burst was seen by the Culgoora spectrograph beginning at 21:30 (and possibly as soon as 21:10 UT) on May 21 following moving metric bursts. It was a continuum with admixture of bursts which could be classified as pure type I noise storm after 23:50 UT. The Culgoora heliograph could image this stationary burst until the end of its observing period at 05 UT on May 22.

The brightness variations at the western arch footpoint indicate a possible correlation with variations in the radio brightness of the type I noise storm at 80 MHz. Thus we suppose that the footpoint variations were produced by particles accelerated high in the noise-storm region and dumped into the low corona and transition layer. Some of these suprathermal particles may be trapped in the X-ray arch, get thermalized there, and provide thus the energy input needed for maintaining constant temperature at the top of the arch. Another source for the continuous supply of energy might be the reconnection of flare loops below the arch which – as other similar events have demonstrated – can continue for many hours. Particles accelerated in the process of reconnection can be trapped in the arch, because the upper disconnected loops are interconnected along the $H_\parallel = 0$ line.

The existence of an arch which is oriented perpendicularly to the flare-loop field lines below it implies an obstacle for any upward motion of the upper loops disconnected in the Kopp and Pneuman (1976) flare model (and any other model of that type). If the arch structure was formed only 15–30 min after the flare onset (when Culgoora first saw it), then this upward motion, i.e. the formation of the coronal transient, had to be fully accomplished before that. If, on the other hand, the arch existed all the time (being perhaps an elevated remnant of that part of the preflare filament which did not erupt), then the Kopp and Pneuman model (and any other model of that nature) seems to be in serious disagreement with observations.

Acknowledgements

References

Acton, L. W., Culhane, J. L., Gabriel, A. H., and 21 co-authors: 1980, *Solar Phys.* **65**, 53.

Allen, C. W.: 1976, *Astrophysical Quantities*, Third revised edition, The Athlone Press, University of London.

Anzer, U. and Pneuman, G. W.: 1982, *Solar Phys.*, in press.

Boelec, A.: 1982, Thesis, State University of Utrecht, The Netherlands.

Brown, J. C.: 1971, *Solar Phys.* **18**, 481.

Culhane, J. L., Gabriel, A. H., Acton, L. W., Rapley, C. G., Phillips, K. J. H., Wolfson, C. J., and 12-co-authors: 1981, *Astrophys. J. Letters* **244**, L 141.

Doyle, J. G. and Raymond, J. C.: 1981, *Monthly Notices Roy. Astron. Soc.*, in press.

Gabriel, A. H., Acton, L. W., Culhane, J. L., Phillips, K. J. H., Wolfson, C. J., Rapley, C. G., and 9 co-authors: 1981, *Astrophys. J. Letters* **244**, L 147.

Gaizauskas, V.: 1981, presentation to the FBS Workshop, GSFC, February 1981.

Hoyng, P., Duijveman, A., Machado, M. E., Rust, D. M., Švestka, Z. Boelee, A., Frost, K. J., Lafleur, H., Simnett, G. M., Van Beek, H. F., and Woodgate, B. E.: 1981, *Astrophys. J. Letters* **246**, L 155.

Kopp, R. A. and Pneuman, G. W.: 1976, *Solar Phys.* **50**, 85.

Kuperus, M. and Van Tend, W.: 1981, paper in preparation.

Moore, R., McKenzie, D. L., Švestka, Z., Widing, K. G., and 12 co-authors: 1979, in P. A. Sturrock (ed.), *Solar Flares*, Proceedings of the Second Skylab Workshop, Colorado Associated University Press, p. 341.

Nolte, J. T., Gerassimenko, M., Krieger, A. S., Petrasso, R. D., and Švestka, Z.: 1979, *Solar Phys.* **62**, 123.

Petrasso, R. D., Nolte, J. T., Gerassimenko, M., Krieger, A. S., Krogstad, R., Seguin, F. H., and Švestka, Z.: 1979, *Solar Phys.* **62**, 133.

Pneuman, G. W.: 1981, *Solar Phys.*, in press.

Raymond, J. C., Cox, D. P., and Smith, B. W.: 1976, *Astrophys. J.* **204**, 290.

Stewart, R. T.: 1976, *Solar Phys.* **50**, 437.

Švestka, Z: 1976, *Solar Flares*, D. Reidel Publ. Co., Dordrecht, Holland.

Švestka, Z., Martin, S. F., and Kopp, R. A.: 1980, in M. Dryer and E. Tandberg-Hanssen (eds.), 'Solar and Interplanetary Dynamics', *IAU Symp.* **91**, 217.

Švestka, Z., Dodson-Prince, H. W., Martin, S. F., Möhler, O. C., Moore, R. L., Nolte, J. T., and Petrasso, R.: 1982a, *Solar Phys.*, in press.

Švestka, Z., Dennis, B. R., Pick, M., Raoult, A., Rapley, C. G., Stewart, R. T., and Woodgate, B. F. 1982b, *Solar Phys.*, submitted.

Van Beek, H. F., Hoyng, P., Lafleur, H., and Simnett, G. M.: 1980, *Solar Phys.* **65**, 39.

Webb, D. F. and Kundu, M. R.: 1978, *Solar Phys.* **57**, 155.

Woodgate, B. E., Tandberg-Hanssen, E. A., Bruner, E. C., and 11 co-authors: 1980, *Solar Phys.* **65**, 73.